Available online at www.sciencedirect.com
ScienceDirect
Cement and Concrete Research 37 (2007) 703–713
Cement and Concrete Research

Damage evolution analysis in mortar, during compressive loading using acoustic emission and X-ray tomography: Effects of the sand/cement ratio

H. Elaqra [a], N. Godin [a], G. Peix [b], M. R'Mili [a,*], G. Fantozzi [a]

[a] Groupe d'Etude de Métallurgie Physique et de Physique des Matériaux, GEMPPM UMR CNRS no. 5510, INSA-Lyon, F-69621, France
[b] Contrôle Non Destructif par Rayonnements Ionisants (CNDRI) INSA-Lyon, F-69621, France

Received 26 June 2006; accepted 12 February 2007

Abstract

This paper explores the use of acoustic emission (AE) and X-ray tomography to identify the mechanisms of damage and the fracture process during compressive loading on concrete specimens. Three-dimensional (3D) X-ray tomography image analysis was used to observe defects of virgin mortar specimen under different compressive loads. Cumulative AE events were used to evaluate damage process in real time according to the sand/cement ratio. This work shows that AE and X-ray tomography are complementary nondestructive methods to measure, characterise and locate damage sites in mortar. The effect of the sand proportion on damage and fracture behaviour is studied, in relation with the microstructure of the material.

Keywords: Mortar; Compression; Damage; Fracture; Mercury porosimetry; Acoustic emission; X-ray tomography

1. Introduction

For its importance in building construction, the concrete has been the subject of several researches the past years. The relationships between microstructure and the mechanical properties are still not well understood; indeed concrete is a heterogeneous and anisotropic material on microscopic scale. With regard to its mechanical behaviour, concrete is often considered as a multi-phases composite structure, consisting of aggregated particles, the cement paste matrix and the interfacial transition zones around the aggregated particles. The mechanical properties of concrete depend strongly on the mix proportion, the grain size distribution, and the preexisting defects like porosity and microcracks. Experimental analysis of damage evolution in composites is not easy, however. A number of nondestructive evaluation techniques have been performed in particular to study the fracture behaviour of concrete under compressive loading. These included acoustic emission [1–6], strain gauge data [7,8] or X-ray tomography [9–12]. X-ray tomography technique has already been used for cement matrix materials, particularly mortars. Landis [9] used a high-resolution 3D scanning technique called X-ray micro tomography to estimate internal crack growth in small mortars cylinders during compressive loading. X-ray tomography is also used to quantify damage parameters of asphalt concrete specimens [11] and to evaluate sulphate attack effects on cement paste [12].

Acoustic emission [13] is a technique capable of real-time damage monitoring. Indeed acoustic emission (AE) is a potential technique to monitor the integrity of materials. In this nondestructive method, ultrasonic waves generated by rapid release of elastic strain energy during damage are detected, collected and analysed. A number of previous studies have evaluated that AE activity is a method for characterizing and locating damage site in concrete materials [14]. Since mortar is a heterogeneous mixture, its cracking process will involve a number of mechanisms on the local scale. The problem that then arises is to determine which of these mechanisms can be identified by AE.

It is generally agreed that the pore structure of concrete or mortar is one of its most important characteristics and strongly influences its properties, particularly with respect to permeability, strength and durability. The effect of concrete porosity on its fracture strength and durability is quite complex. The pore network can be penetrated by mercury intrusion porosimetry (MIP);

* Corresponding author. Tel.: +33 472436127; fax: +33 472438528.
E-mail address: Mohamed.Rmili@insa-lyon.fr (M. R'Mili).

0008-8846/$ - see front matter © 2007 Elsevier Ltd. All rights reserved.
doi:10.1016/j.cemconres.2007.02.008

Table 1
Chemical analysis of the Portland cement

Constituent	%	Constituent	%
SiO_2	22.8	C_3S	65.5
Al_2O_3	2.7	C_2S	15.8
Fe_2O_3	1.9	C_3A	3.9
CaO	63.8	C_4AF	5.9
MgO	0.8	$CaSO_4$	3.7
Na_2O	0.2	CaO libre	1.0
Na2O	0.2	P_2O_5	0.2
TiO_2	0.1	K_2O	0.2
Mn_2O_3	0.1	SrO	0.1

however MIP cannot indicate the pore shape or the position of the pores [15–17] which are important for analysing the fracture behaviour of concrete. The general appearance of two-dimensional images of pores is visualised by using scanning electron microscopy (SEM). SEM is a direct method to characterise pore structures in concrete. Pores structures in cement pasts and concretes have been evaluated by this technique [18–20]. The sizes of pore diameters detected by this method are much greater than those by the MIP method. At highest magnifications, it is possible to observe the morphology of the calcium silicate hydrate gel (C–S–H) and pores size down to about 100 nm. During the hydration process, the anhydrous cement grains react with water to produce hydrates. In the Portland cement paste, the hydration reaction is dominated by the reaction of the calcium silicate (C_2S), which produces hydroxide (CH) and calcium silicate hydrate gel. The deposition of these phases in the microstructure is quite distinct, CH precipitates in the water filled pores while C–S–H deposits mainly around the cement grains. The characteristics of the interfacial zone may be affected by a chemical reaction between the aggregates and the cement paste.

The effects of the s/c ratio on fracture behaviour of mortar were experimentally studied in this paper. Several methods and especially AE and X-ray tomography were used to asses the preexisting defects, the damage evolution and the fracture of the specimens under compressive loading. Mechanical tests were performed on various specimens with s/c ratios varying from 1 to 4. The porosity and microcracks were first visualised by using SEM. Then mercury intrusion porosimetry was used to evaluate the microporosity. Complementary data on the pores sizes distribution was obtained using X-ray tomography. During mechanical tests, AE events have been collected and analysed in order to evaluate the microcracking process and damage accumulation in mortar materials.

2. Experimental procedures

2.1. Materials and mix proportion

The cement used was Lafarge Portland cement (HTS 52, 5 PMES). Its chemical composition is given in Table 1. The specimens were prepared with a water-to-cement (w/c) weight ratio equal to 0.50. The aggregates used were standard sand with a maximum grain size of 2 mm. In order to investigate the effect of sand to cement ratio on the mechanical properties of concrete, three sand-to-cement (s/c) weight ratios were mixed: 1:1, 3:1 and 4:1. Casting and curing of the specimen are conducted in laboratory environment. The sand and the cement were mixed for 5 min. Water is slowly added while the dry materials are being mixed and then the mixture is stirred with water for 10 min. After 10 min, the mould is vibrated on a table vibrator. Mortar cylinders of 120 mm in length and 30 mm in diameter were produced. After casting, the specimens were sealed in plastic bags to prevent moisture loss and stored in laboratory environment for 2 days. Thereafter the cylinders were demoulded and the specimens were cured in water at 20 °C until the age of 28 days.

2.2. Mechanical testing

In order to study the history damage history of concrete under compression testing, concrete cylinders of 60 mm in length were

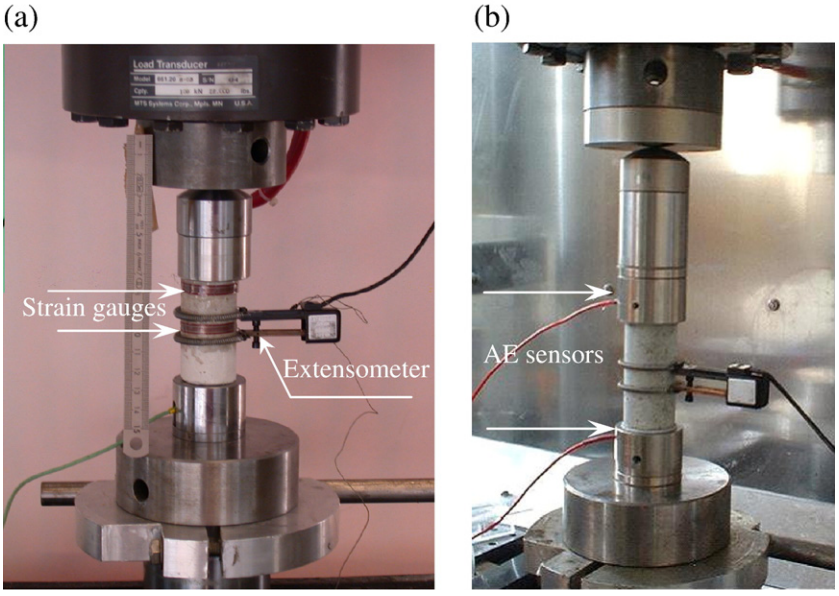

Fig. 1. View of the set-up for uniaxial compression: specimen with (a) strain gauges and (b) AE sensors.

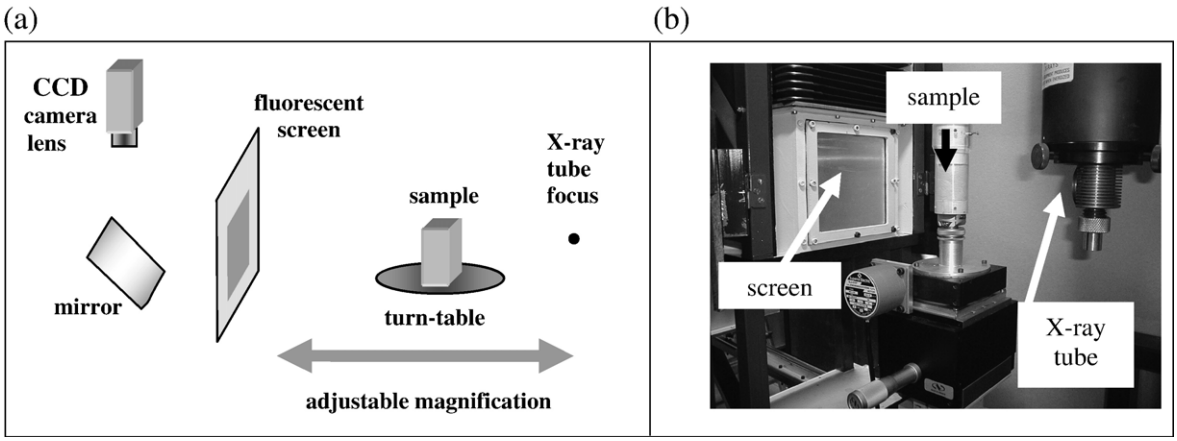

Fig. 2. General scheme of the scanner: (a) principle; (b) the sample on its turn-table.

cut from the central portions of the specimens. All the tests were performed by using an experimental set-up as shown in Fig. 1. The top and the bottom of the specimen are embedded by silicon grease to reduce friction between specimen surfaces and plates. The uniaxial compression tests were conducted using a servo-hydraulic MTS model 810 testing machine equipped with a 100 kN load-cell. The displacement rate used was 2 μm/s. Strain gauges with a gauge length of 30 mm were used. The axial elongation was measured by using an extensometer with a 12.5-mm gauge length. To follow the variation of transverse extension during the loading test, two strain gauges of Kyowa KFG 30-120-C1-11 type with a gauge length of 30 mm were mounted in the top and in the middle position of gauge length as shown in Fig. 1a.

2.3. Specimens preparation

The scanning electron microscopy (SEM) investigation is used to observe the microcracks, the pore shapes and sizes and surface texture. It is important to ascertain that no cracks are introduced during preparation of the specimens. Indeed, the sample were dried in drying oven at 30 °C and then impregnated with a low viscosity epoxy (EPO-TEK 301). After the epoxy had cured for 24 h at 40 °C, the specimens were polished with diamond grit of progressively finer sizes down to 0.25 μm. Mercury intrusions porosimetry (MIP) was also used on cement mortar specimens to analyse pores size distribution of the bulk material. The MIP test was carried out on a Micrometrics 9300 system with a maximum of 400 MPa injection pressure. Specimens of about 4 g were sampled in the middle part. The mercury intruding pore diameter d at pressure P was calculated using the Washburn equation: $d=-\gamma\cos\theta/P$, where γ is the surface tension of mercury (0.484 N/m) and θ is the contact angle between mercury and the pore wall (130°).

2.4. Acoustic emission instrumentation

A two-channel Mistras 2001 data acquisition system of Physical Acoustics Corporation (PAC) with a sampling rate of 8 MHz and a 40-dB preamplification was used to record AE. The total amplification of the recording system was 80 dB. Ambient noise was filtered using a threshold of 42 dB. AE measurements were achieved by using two resonant micro-80 PAC sensors which have a resonant frequency around 250 kHz, coupled on the bases of the cylinders with silicon grease (Fig. 1b). The amplitude distribution covers the range 0–100 dB (0 dB corresponds to 1 μV at the transducer output). The nominal distance between the sensors was 60 mm or 100 mm. After installation of the

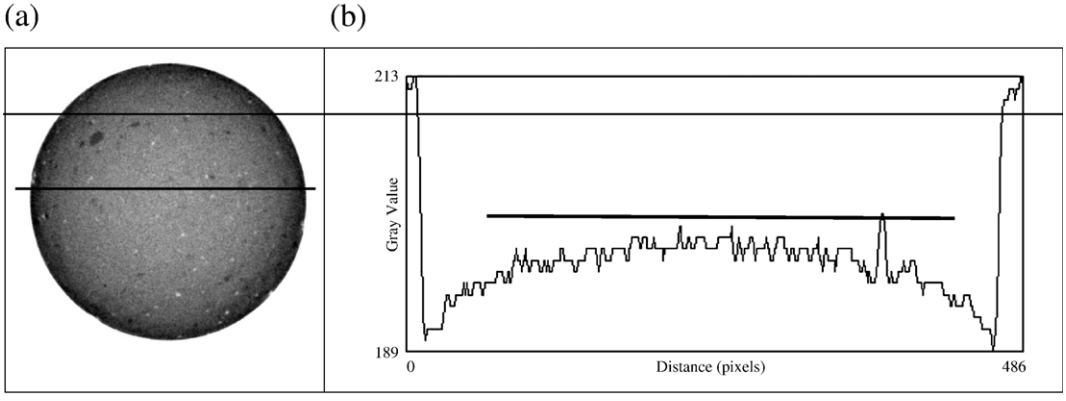

Fig. 3. Image of a slice within the sample characterized by s/c = 1. (a) Grey-level image of the slice: pores correspond to the white small spots while cements agglomerates are seen as darker areas. (b) Grey-level profile along the oriented line selected in (a).

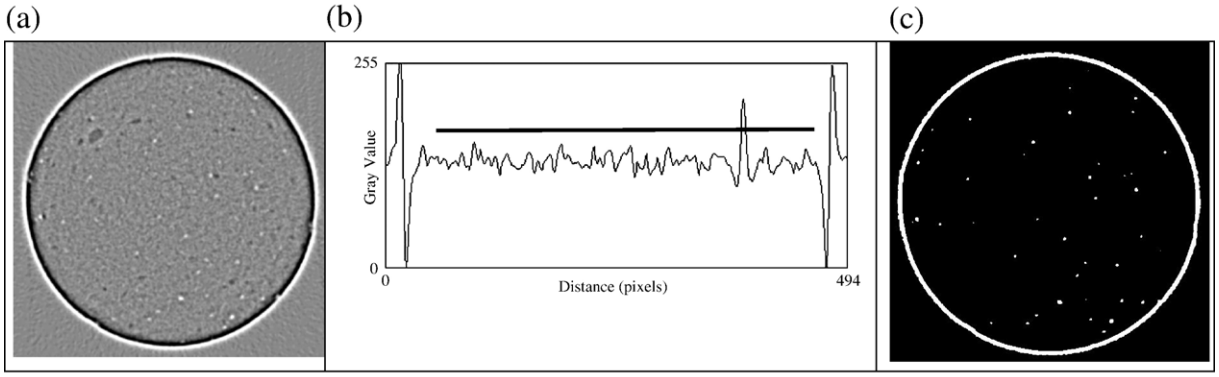

Fig. 4. Pore detection within the slice after band-pass filtering of Fig. 3a. (a) Grey-level image after a band-pass filtering. (b) Profile along the line selected in Fig. 3a. (c) Segmentation of pores.

transducers, a pencil lead break procedure was used to generate repeatable AE signals for the calibration of each test. So the acquisition parameters have been set as follows: peak definition time (PDT)=100 μs, hit definition time (HDT)=200 μs and hit lock time (HLT)=1000 μs. Velocity and attenuation of waves have been measured several times for each kind of specimens. The velocity is required to localise the AE sources from the difference in arrival times between the two sensors (around 3500 m/s). We did not observe an evolution of the wave's velocity with the s/c ratio. The relation between the measured peak amplitude and the distance between the pencil break and the sensor shows that the reduction of the peak amplitude is approximately 100 dB/m. This value is quite large compared to the attenuation in steel, but is typical in concrete. After the calibration step, AE was continuously monitored during tensile tests. For each captured signal, a procedure of source localisation was performed. In order to avoid irrelevant influences, only AE signals from events located between the sensors are processed. Six parameters were calculated for each signal from the waveforms: amplitude, duration, rise time, counts, counts to peak and energy. Furthermore, each waveform was digitised and stored.

2.5. X-ray tomography

2.5.1. Physical principles of X-ray tomography

X-ray tomography allows the non invasive evaluation of materials for a large set of purposes [21,22]. The usual technique, named *transmission tomography* or *attenuation tomography*, is based on the measurement of X-ray attenuation

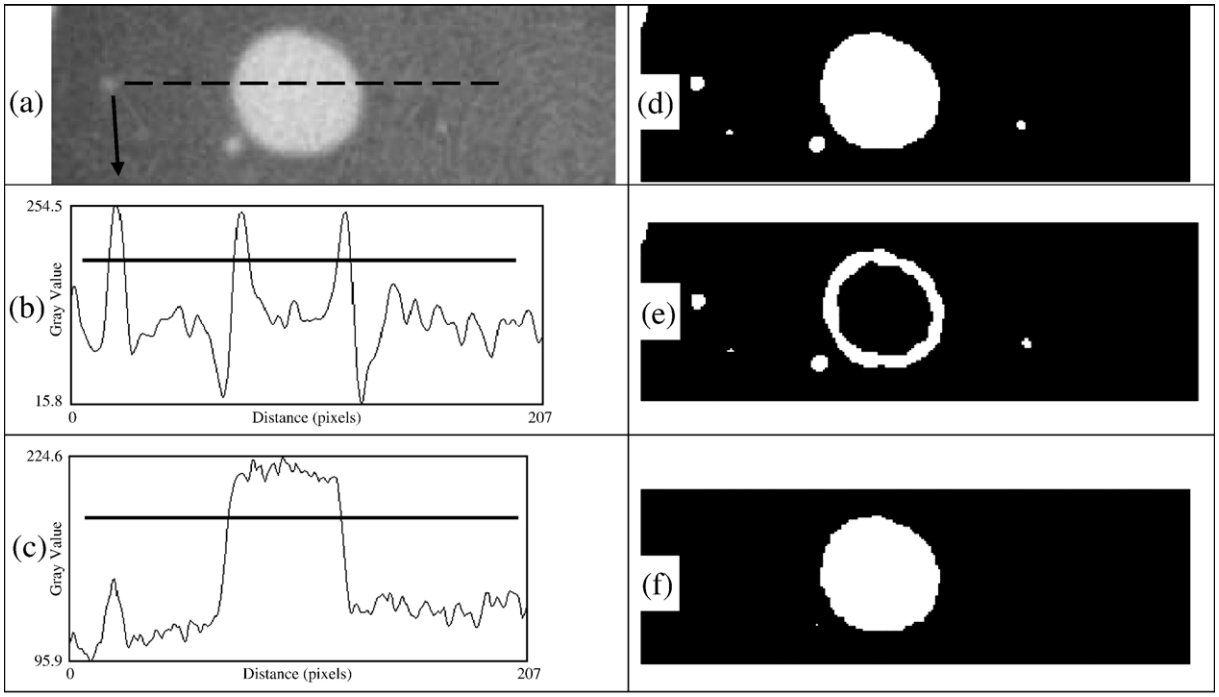

Fig. 5. Detection of big and small pores: (a) Grey-level tomographic initial image. (b) Profile within the band-pass-filtered version of (a). (c) Profile within the initial image (a). (d) Segmented final image (binary summation of (e) and (f)). (e) Segmentation of the band-pass-filtered image. (f) Segmentation of the initial image.

along a set of directions throughout the evaluated object. For that purpose, a set of radiographic images, named *projections*, are captured, corresponding to different possible directions of irradiation. For every sensitive pixel in the detector and every angular step of the turntable, the measured intensity is given by the Beer–Lambert law:

$$I = I_0.\exp\left(-\int_{\text{ray path}} \mu(x)\ \mathrm{d}x\right)$$

where $\mu(x)$ stands for the attenuation coefficient along the ray path inside the inspected material. Measuring I and I_0 with the imaging device, we are then able to determine the integral of $\mu(x)$ along a great number of paths. This set of integrals is known as the *Radon transform* of the μ map of the object. Provided the Radon transform is reasonably well sampled, the *projection–slice theorem* allows the resolution of the inverse problem, i.e. the establishment of the μ map. In our case, image reconstruction is effected using the three-dimensional FBP (filtered back-projection) algorithm of Feldkamp [23,24]. The computed μ values are correlated to the local density and chemical composition of the investigated sample.

2.5.2. Description of the X-ray scanner

A scanner was conceived and constructed in the laboratory CNDRI. The general purpose was high resolution 3D imaging of the internal structure of any material, within a large range of spatial resolutions. The scanner is mainly constituted with a micro focus X-ray tube (Philips 161 HOMX) and an X-ray sensitive imager. The small size of the X-ray tube focus allows geometrical magnification of the image, while maintaining a low value of the *image blurring* (also denoted *geometrical unsharpness*). Changing the magnification allows the adaptation of the spatial resolution of our scanner to different applications. The effective voxel size within the reconstructed image can be chosen between 15 and 100 μm. The imager, a low noise CCD camera (Charge-Coupled Device), cooled by a triple-stage Peltier cooler and equipped with a high-aperture lens is used to catch the weak visible image emitted by a terbium-doped gadolinium oxysulfide (Gd_2O_2S [Tb]) fluorescent screen. The scheme of the constructed device and a photograph of the scanner are displayed in Fig. 2.

2.5.3. Choice of the experimental conditions

For the proposed application, a voxel value of 65 μm for the reconstructed image was selected. The corresponding 3D image format ($500 \times 500 \times 882$ voxels^3) is thus able to completely describe a concrete sample 30 mm in diameter and 53 mm in length (central active part). The spatial accuracy is sufficient and the computation times remain acceptable: a few hours for the 3D image reconstruction and a few seconds for the segmentation of the voids inside the whole volume. Due to the high density of concrete and high atomic number of its mineral parts, a 100 kV value of the X-ray tube potential was chosen. A copper filter, 0.3 mm in thickness, was directly set at the tube window, thus allowing the selective absorption of the lower energies components of the spectrum. The aim of such an arrangement is to reduce the "beam-hardening" artefacts which are due to the progressive change in the mean beam energy, throughout the sample [25]. Under such conditions, the corresponding mean-energy of the filtered beam can be estimated to be in the range 60–70 keV. The distance between focus and screen was 355 mm and the magnification 1.5 (corresponding to the selected effective desired voxel size). Using a tube current of 0.15 mA, the overall acquisition and readout time for each of the 720 projections was 17 s (3.5 h for the scan).

2.5.4. Validation of the technique

Fig. 3a displays the tomographic image of an arbitrary slice within an investigated concrete sample corresponding to the

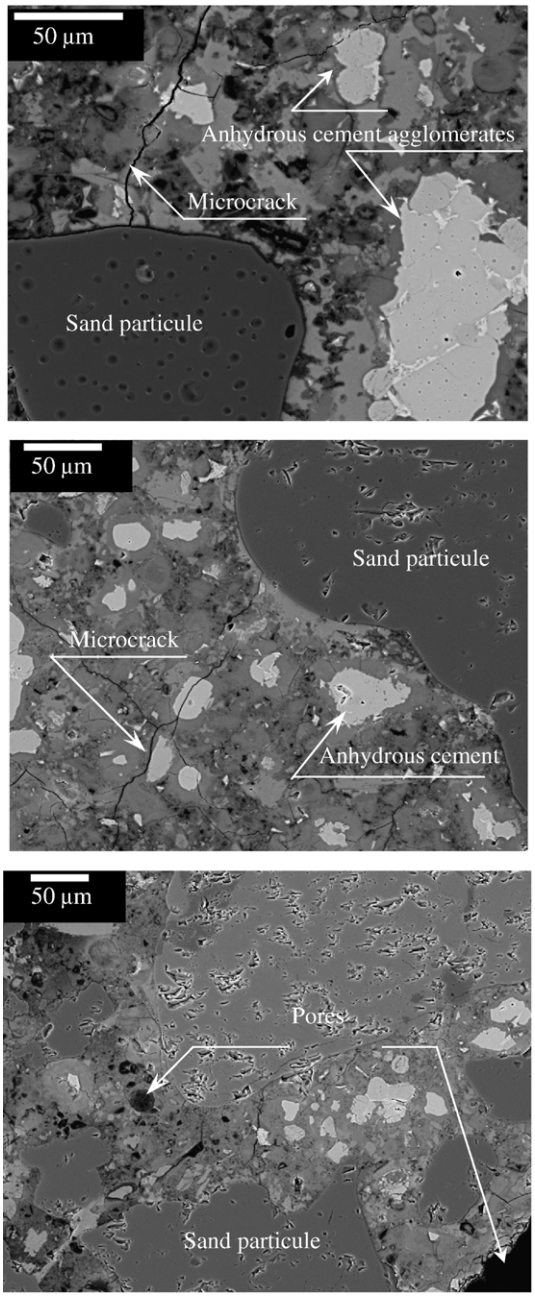

Fig. 6. SEM view of the microstructure of virgin specimens for s/c = 1, 3 and 4, respectively.

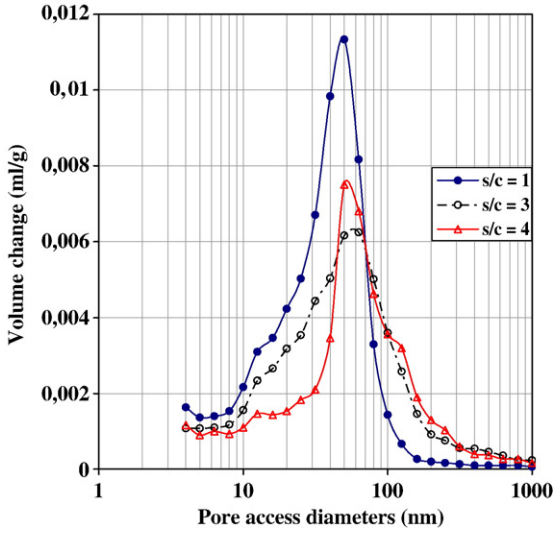

Fig. 7. Pore size distribution for a sand to cement ratio of 1, 3 and 4.

ratio s/c = 1. Different phases are observed within concrete; pores are characterised, like surrounding air, by a white tone. Unfortunately the baseline of the grey level profile is not constant throughout the sample, as can be seen in Fig. 3b. The curved shape of the baseline, named "cupping effect", which corresponds to an incomplete correction of the beam-hardening, prevents a direct discrimination of the small pores located in the peripheral region.

Correction of beam-hardening (and therefore suppression of the cupping effect) can be effected by preprocessing the projection images just before the reconstruction step. In this case, a calibration of the individual projection images must be effected, by reference with a nondefective and homogeneous sample [22]. This linearisation method being complex and time-consuming, we preferred a post-processing of the reconstructed slices. We therefore applied a band-pass filter, acting in the Fourier domain, on the images of the slices. Fig. 4a displays the image of the same slice after processing: the images of small pores are preserved. Fig. 4b shows the corresponding profile along the same line: the cupping effect has disappeared and an easy segmentation is therefore possible, delivering an image of pores which is consistent with the reality Fig. 4c and Fig. 3a will be compared for this purpose. It can be noted that the profile is corrupted in the peripheral area of the specimen: remaining high-frequency components are responsible for such behaviour. Therefore all the results presented in this paper will be representative only of the central part of the sample. An additional problem appears when considering concrete samples with an s/c ratio equal to 3. In these compounds, big air voids are present, as shown in Fig. 5a. Under those conditions, the segmentation of

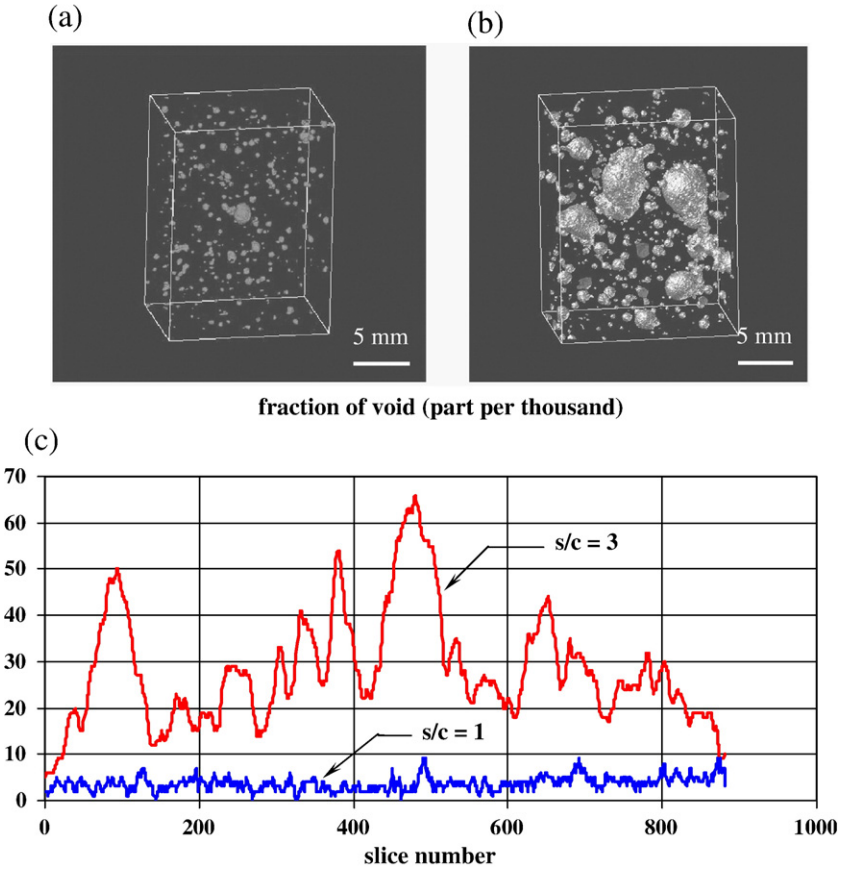

Fig. 8. Porosity estimation using tomographic investigation within two different compounds characterized by s/c ratios of 1 and 3. (a) 3D image of compound with s/c = 1; red blocks correspond to porosities. (b) 3D image of compound with s/c = 3; red blocks correspond to porosities. (c) Fraction of voids along the 882 slices of both compounds. (For interpretation of the references to colour in this figure legend, the reader is referred to the web version of this article.)

the treated image enhances only the small voids and the peripheral part of the big ones (Fig. 5b and e). A further segmentation, directly applied on the initial image is necessary (Fig. 5c and f). Both segmented images, which are binary, are then added to deliver the final image (Fig. 5d). Segmentation levels are shown in Fig. 5b and c.

3. Results and discussion

3.1. Microstructure

The following section presents the results and analysis derived from the SEM investigations, the MIP tests and the X-ray tomography. SEM examinations were carried out on the flat-polished section. Fig. 6 shows the SEM micrographs of surface texture of mortar materials. In this figure we can distinguish residual unhydrated Portland cement particles, porosity and microcracks. In cement-based materials microcracks are usually observed, they are formed during drying and are the result of thermal shrinkage mismatch of sand particles and cement paste. Mortar of s/c=1 exhibited more extensive microcracking than high s/c ratio concrete in undamaged condition. The size of anhydrous cement agglomerates decreases with the s/c ratio. Moreover, our observations indicate that the size of the porosity in the bulk material increases with the s/c ratio. Less than 100 μm for s/c=1 and higher for s/c=3 and 4.

Fig. 7 shows the results of pore size distribution curves from MIP with various s/c ratios. This figure exhibits pore size distributions curves. The mortar with s/c=1 has a very narrow porosity distribution peak with mean values centred on 50 nm. But mortars with s/c=3 and 4 are in the same range in pore size distribution with large pore diameters. The total porosity reached by the MIP technique decreased with s/c ratios from 17% to 10%.

The image of the 3D pore within concrete is shown in Fig. 8 for two different sand/cement ratios: 1 and 3. Using this technique it is possible to detect those pores whose diameter exceeds roughly 250 μm (4 voxels). Fig. 8a and b display 3D images of significant sub-volumes extracted from both compounds. Air voids correspond to the light grey volume. Fig. 8c displays the fraction of voids of both volumes along the 882 investigated slices. It is thus observed that the specimen with the s/c ratio equal to 3 presents larger pores with a large scattering. The fractions of void vary strongly and randomly along the sample (between 10 and 60%). The reduction of the total porosity and scattering appears for specimen with the s/c ratio equal to 1. X-ray tomography investigations show that pore size and the total porosity decrease with s/c ratios. It is clear that the results of pores size distribution depend strongly on the length scales involved and on the technique used. By means of MIP, pores between about 2 nm and up to about 100 μm can be observed.

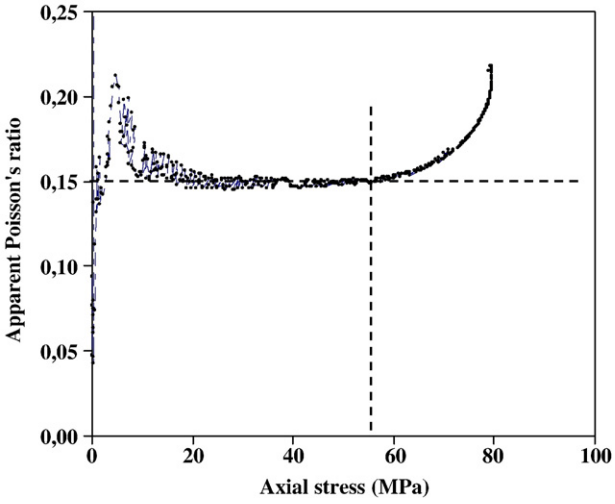

Fig. 10. Relationship between axial stress and apparent Poisson's ratio for a specimen with s/c=3.

The MIP tests, the X-ray tomography and the SEM examinations are complementary techniques to investigate cement based materials. MIP is a nondirect measurement technique to give bulk information about accessible pore sizes less than 100 μm, but MIP investigations cannot indicate the shape or the position of the pore [16].

3.2. Mechanical response

In this part particular attention is given to the fracture process and damage history. Fig. 9 shows a typical stress–strain diagram

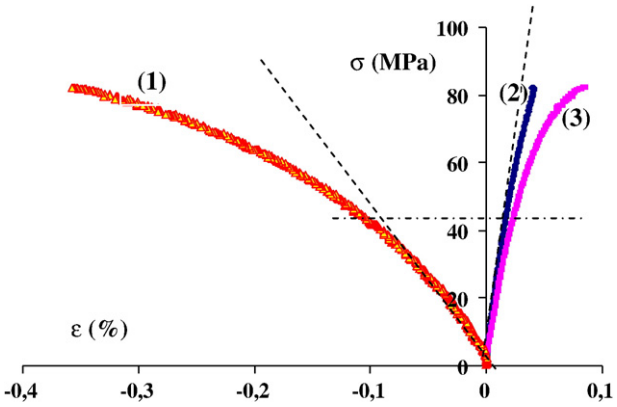

Fig. 9. Typical stress–strain curves for a sand to cement ratio of 3.

Fig. 11. Failure mode under uniaxial compression.

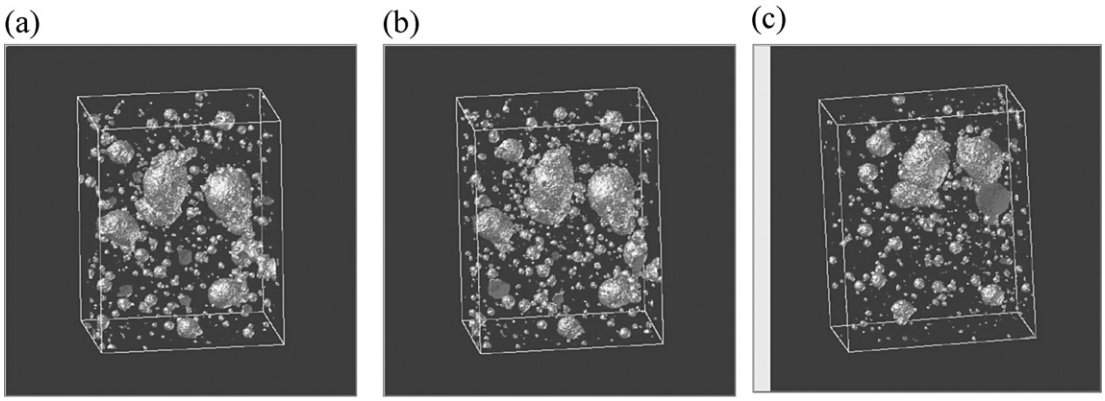

Fig. 12. 3D images of the concrete sample (s/c=3) under three successive states of compressive stress: (a) without loading, (b) loaded up to 10 MPa and (c) 60 MPa.

of mortar with s/c=3. The negative strain branch corresponds to the longitudinal compressive strain (curve (1)). The positive strain branches of the stress–strain diagrams in Fig. 9 correspond to the transverse extension collected at the top (curve (2)) and at the mid-height of the specimen (curve (3)). Both transverse extensions exhibit linear and similar responses up to 45 MPa, i.e., 56% of stress–strength ratio. This behaviour indicates that strain fields are uniform along of the specimen. We can observe that transverse extension at the mid-height of the specimen increases much more than that collected at the top of the specimen. This change is the result of the sum of the elastic behaviour due to Poisson's ratio effects and the dilation due to the microcracking (nonelastic part). It has been experimentally observed [7,26] that the beginning of significant microcracking is indicated by the beginning of an increase in the apparent Poisson's ratio (ν_p) which is the sum of elastic part and nonelastic contribution. Indeed, when the load reaches its maximum, microcrack increases rapidly and lateral expansion is significant, so ν_p increases in a significant way. Fig. 10 shows the relationship between axial stress and apparent Poisson's ratio, which is the ratio of the lateral strain to the axial strain. With the exception of high scattering at the initial loading due to higher percentage error of strain measurements, ν_p is a constant value of about 0.16 for stresses smaller than approximately 60 MPa i.e. 75% of stress–strength ratio, and increases with the growth of microcracks and becomes unstable until failure. We should notice here (Figs. 9 and 10) that a significant increase of ν_p appears after the pseudo-yield stress of material (45 MPa). It is observed (Fig. 9) that a rapid increase of ν_p occurs when lateral expansion is significant, which is in agreement with the literature. Thereafter apparent Poisson's ratio will be taken as indicator to prevent the beginning of unstable cracks growth. With the increase in the load, failure of the sample occurs in quasi-brittle manner at about 85 MPa. A typical failure mode under uniaxial compression is shown in Fig. 11.

To follow the change of the internal voids in relation with the load levels, three strain states of the sample with s/c ratio equal to 3 are investigated by X-ray tomography. In this study, the tomographic scan does not need to be made in real time during loading, thus the results of X-ray tomography according stress levels can be attributed to the irreversible mechanisms. Fig. 12 displays a partial 3D view of the internal voids within the three strain states of the sample. Fig. 12a and b show that the voids are nearly unchanged in the undamaged specimen and in the specimen loaded up to 10 MPa. On the contrary, the internal voids change significantly in the third state of load as shown in

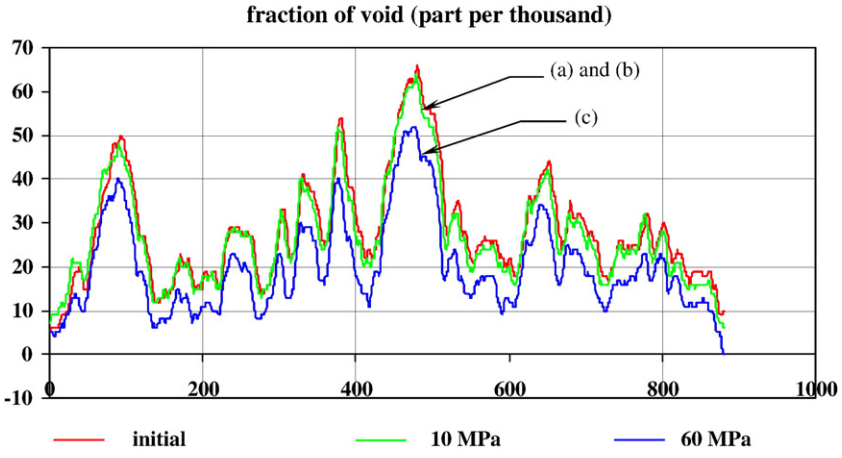

Fig. 13. Fraction of voids along the 882 slices of the concrete sample (s/c=3) under three successive states of compressive stress: (a) without loading, (b) loaded up to 10 MPa and (c) 60 MPa.

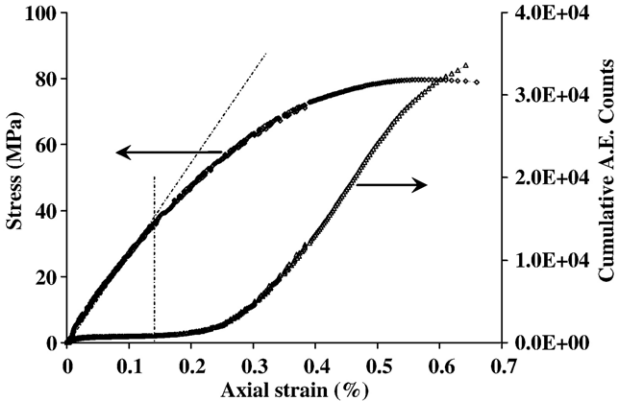

Fig. 14. Stress–stain curve and cumulative AE counts for a sand to cement ratio of 3.

Fig. 12c. This figure shows that some cavities disappear: these are then converted into microcracks which are too small to be detected by our X-ray tomography equipment. Interconnections between large pores "fracture of walls" are observed (circled on Fig. 12c) and they can be regarded as relaxation sites of fracture energy. Note that in the region outside circles, the number of pores decreases significantly. These observations suggest that a closing process occurs at the beginning of the nonlinear behaviour and that it is related particularly to the pores of small size. Air voids seem to provide favourable locations for multiple crack branching [27]. It is obvious that crack growth is influenced by the number and the sizes of the original voids in the specimen.

Fig. 13 shows the corresponding quantitative investigation of the pores distribution along the specimen length. It is clear that no change appears between the first and the second state of the load. On the contrary, for the specimen loaded until 60 MPa, the internal voids decrease of about 10% in a uniform manner throughout the compression specimen. Results from these observations and measurements revealed to be useful in interpreting how the fracture mechanisms play a role in governing damage and fracture behaviour under compressive loading.

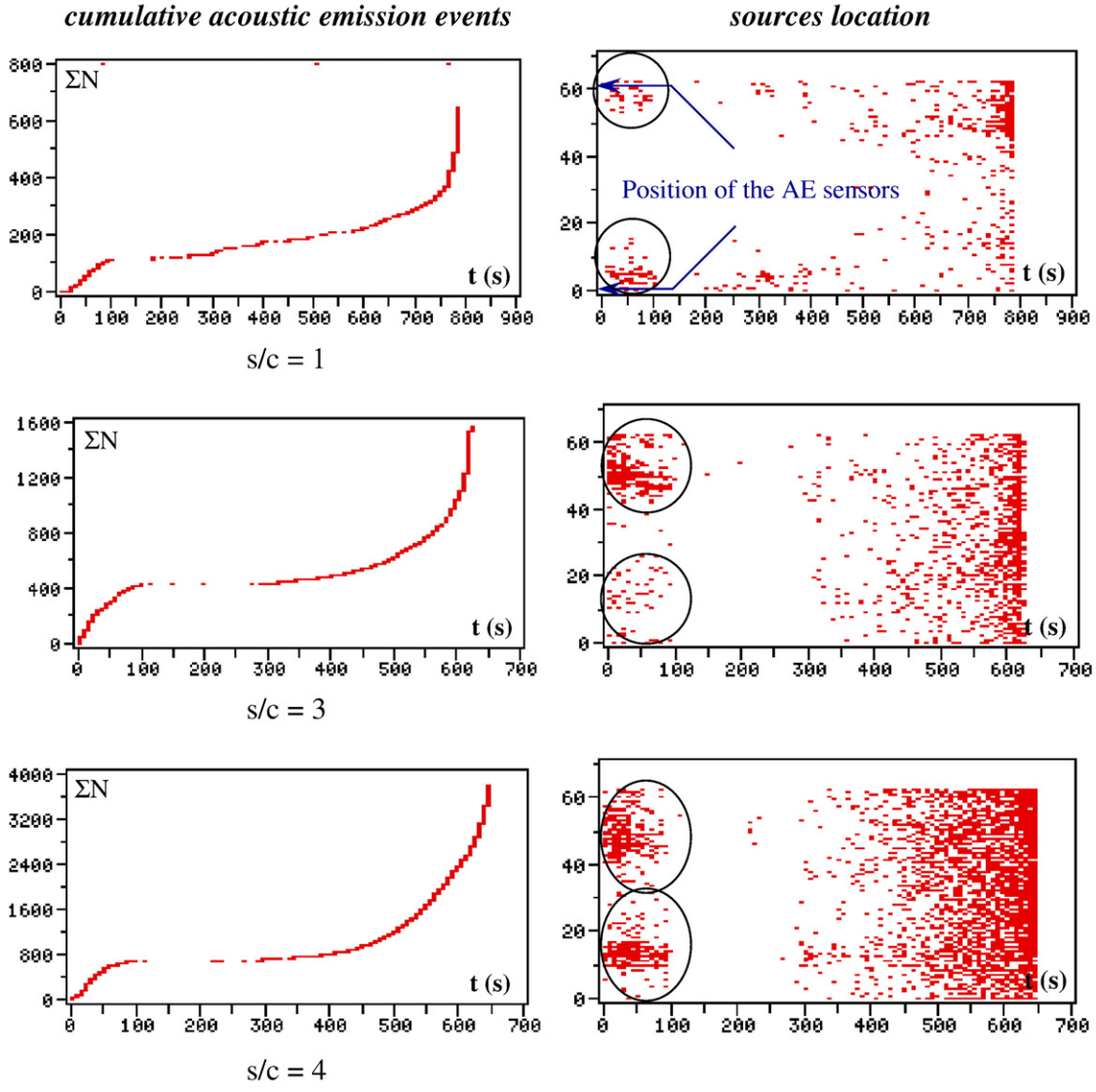

Fig. 15. Effect of sand proportion on cumulative acoustic emission events (Σ*N*) and sources' location.

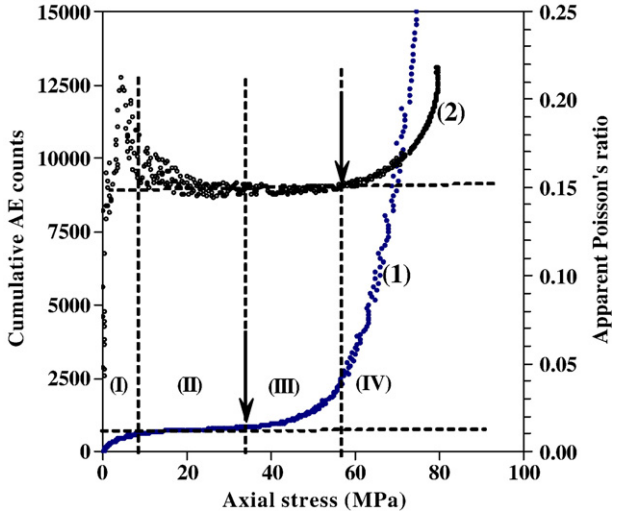

Fig. 16. Relationship between (1) cumulative AE counts and (2) apparent Poisson's ratio during compressive loading of specimen with s/c=3.

3.3. Acoustic emission history

In this study, only cumulative AE counts are used. The first approach discussed in this part investigates the number of acoustics emission signals generated during the compressive loading. Fig. 14 shows a typical stress–strain curve and the cumulative AE counts collected using only one sensor mounted on the bottom surface of the specimen. This figure shows some zones which are characterised by the rate of AE activities. To describe the damage mechanisms in relation with stress levels, the locations of the AE sources were evaluated. Fig. 15 shows the linear positions of the AE sources between the sensors versus the time for sand to cement ratio equal to 1, 3 and 4, respectively. It was found that all the specimens exhibit a significant common trend of the variation of the AE activity as a function of time. So failure of the specimens is governed by the same fracture processes. For all the tests, it should be noted that the initial AE source locations are distributed near the ends of the sample (circled on Fig. 15). After a silence zone, AE activity increases in a continuous way until failure of specimen. It was also shown in this figure that the number of AE events increases significantly with the sand to cement ratio, indicating that the AE sites are preferentially localised along the sand to cement interfaces. However, AE signals and visual observations of defects found that the damage level in mortar material corresponds to the pores closing, interconnection of the pores, multiple crack branching and sand to cement interfaces cracking. The results of X-ray tomography, strain gauges data and acoustic emission can be used better to understand and quantify the general relationship between stress levels and cracks development in the mortar material. The use apparent Poisson's ratio and AE activities as function of stress level (Fig. 16) which can be divided into four stages, namely:

- Stage (I): At the beginning of the test, many AE signals were detected. In this stage AE events are particularly located in the neighbouring of the ends of specimen, it can be associated to the local crack closure.
- Stage (II): Linear-elastic behaviour: in this stage, called "silence zone", no AE signals were detected. Indeed, once that the majority of existing cracks located on the end of the specimen are closed and linear-elastic behaviour takes place.
- Stage (III): Stable crack growth: when the stress–stain curve becomes nonlinear, a rapid increase of AE events occurs. These AE activities can be attributed to the local degradation such as pores closing, interconnection of the large pores, multiple crack branching and sand to cement interfaces cracking.
- Stage (IV): Unstable crack growth: when the specimen approaches its ultimate strength, it is assumed that the unstable cracking occurs by interconnection between the defects which are created in the third stage. Therefore, the apparent Poisson's ratio increases significantly up to the failure.
- It is clear that in fact the fracture processes operate at the third stage which seems to control the lifetime of the mortar material. Using X-ray tomography and cumulative AE counts, one cannot describe in a reliable way either the chronology or the proportion of the fracture processes referred to above. The multiparameter filtering and clustering procedure is still under progress. Indeed, the parametric AE data will allow us to better understand the fracture mechanisms during a compressive loading [28,29].

4. Conclusions

From the results presented in this paper it can be concluded that:

- X-ray tomography, strain gauges data and acoustic emission can be used to understand and quantify the general relationship between stress level and cracks development in the mortar material.
- On a meso-scale, X-ray tomography can be a powerful tool for investigating complex materials such as mortar or concrete. 3D image analysis gives important information, in particular pores size distribution and evaluation of internal voids change with sand proportion and during compressive loading on concrete specimens.
- Acoustic emission was found as the efficient technique to follow damage history in cement-based materials.
- To describe fracture process in a realistic manner, it is necessary to take into account all information of the nano-, micro- and meso-scale.

Acknowledgement

We thank the CEA-LETI (Grenoble-France) which allowed the free disposition of "eve_recons", tomographic reconstruction software.

References

[1] E.N. Landis, Micro–macro fracture relationships and acoustic emission in concrete, Construction and Building Materials 13 (1999) 65 – 72.
[2] M. Ohtsu, H. Watanabe, Quantitative damage estimation of concrete by acoustic emission, Construction and Building Materials 15 (2001) 217–224.

[3] T. Shiotani, M. Shiotani, M. Ohtsu, Acoustic emission of concrete pile, Construction and Building Materials 13 (1999) 73 – 85.
[4] K. Wu, B. Chen, W. Yao, Study of the influence of aggregate size distribution on mechanical properties of concrete by acoustic emission technique, Cement and Concrete Research 31 (2001) 919 – 923.
[5] Ken Watanabe, Junichiro Niwa, Mitsuyasu Iwanami, Hiroshi Yokota, Localized failure of concrete in compression identified by AE method, Construction and Building Materials 18 (2004) 189 – 196.
[6] Bing Chen, Juanyu Liu, Effect of aggregate on the fracture behaviour of high strength concrete, Construction and Building Materials 18 (2004) 585–590.
[7] Y.H. Loo, Propagation of microcracks in concrete under uniaxial compression, Magazine of Concrete Research 47 (1995) 83 – 91.
[8] C.C. Lim, N. Gowripalan, V. Sirivivatnanon, Microcracking and chloride permeability of concrete under uniaxial compression, Cement and Concrete Composites 22 (2000) 353–360.
[9] E.N. Landis, N.N. Edwin, D.T. Keane, Microstucture and fracture in three dimensions, Engineering Fracture Mechanics 70 (2003) 911–925.
[10] E.N. Landis, N.N. Edwin, Three-dimensional work of fracture for mortar in compression, Engineering Fracture Mechanics 65 (2000) 223–234.
[11] L.B. Wang, J.D. Frost, G.Z. Voyiadjis, T.P. Harman, Quantification of damage parameters using X-ray tomography images, Mechanics of Materials 35 (2003) 777–790.
[12] S.R. Stock, N.K. Naik, A.P. Wilkinson, K.E. Kurtis, X-ray microtomography (microCT) of the progression of sulfate attack of cement paste, Cement and Concrete Research 32 (2002) 1673–1675.
[13] A.G. Beattie, Acoustic emission, principles and instrumentation, Journal of Acoustic Emission 2 (1983) 95–128.
[14] Taketo Uomoto, Application of acoustic emission to the field of concrete engineering, Journal of Acoustic Emission 6 (1987) 137–144.
[15] D.N. Winslow, S. Diamond, A mercury porosimetry study of the evolution of porosity in Portland cement, Journal of Materials 5 (1970) 564–585.
[16] S. Diamond, Mercury porosimetry: an inappropriate method for the measurement of pore size distributions in cement-based, Cement and Concrete Research 23 (2001) 1517–1525.
[17] C. Gallé, Effect of drying on cement-based materials pore structure as identified by mercury intrusion porosimetry: a comparative study between oven-, vacuum-, and freeze drying, Cement and Concrete Research 31 (2001) 1467–1477.
[18] S. Diamond, Jingdong Huang, The ITZ in concrete – a different view based on image analysis and SEM observations, Cement and Concrete Composites 23 (2001) 179 – 188.
[19] S. Diamond, Aspects of concrete porosity revisited, Cement and Concrete Research 29 (1999) 1181–1188.
[20] L. Karen Scrivener, Backscattered electron imaging of cementitious microstructures: understanding and quantification, Cement and Concrete Composites 26 (2004) 935 – 945.
[21] J. Baruchel, X-ray Tomography in Material Science, Hermes-Science, Paris, 2000.
[22] N. Douarche, D. Rouby, G. Peix, J.M. Jouin, Relation between X-ray tomography, specific gravity and mechanical properties in carbon–carbon composites braking applications, Carbone 39 (2001) 1455 – 1465.
[23] L.A. Feldkamp, L.C. Davis, J.W. Kress, Practical cone-beam algorithm, Journal of the Optical Society 1 (1984) 612 – 619.
[24] A.C. Kak, M. Slaney, Computerized Tomographic Imaging, IEEE Press, New York, 1987.
[25] P. Grangeat, La Tomographie, Hermes-Science, Traité IC2, Paris, 2002.
[26] A.B. Toader, E. Spacone, M. Kwon, A 3D hypoplastic model for cyclic analysis of concrete structures, Engineering Structures 23 (2001) 333–342.
[27] S. Mindess, S. Diamond, The cracking and fracture of mortar, Matériaux et Constructions 15 (1982) 107–113.
[28] N. Godin, S. Huguet, R. Gaertner, Integration of the Kohonen's self-organising map and *k*-means algorithm for the segmentation of the AE data collected during tensile test on cross-ply composites, NDT & E International 38 (2005) 299 – 309.
[29] M. Moevus, N. Godin, M. R'Mili, D. Rouby, P. Reynaud, G. Fantozzi, Acoustic emission data clustering and damage mechanisms identification in a SiC/[Si–B–C] composite, in: J. Lamon, A.T. Marques (Eds.), Proc. of the 12th Europ. Conference on composite Materials (ECCM12). Biaritz 29th August - 1st September, 2006.